JGR Solid Earth

RESEARCH ARTICLE
10.1029/2021JB022313

# Impact Versus Frictional Earthquake Models for High-Frequency Radiation in Complex Fault Zones

**Victor C. Tsai[1], Greg Hirth[1], Daniel T. Trugman[2], and Shanna X. Chu[1]**

[1]Department of Earth, Environmental and Planetary Sciences, Brown University, Providence, RI, USA, [2]Jackson School of Geosciences, University of Texas at Austin, Austin, TX, USA

**Key Points:**

- We compare the predicted earthquake ground motions from elastic impacts in a complex fault zone with predictions from frictional models
- Ground motions from elastic impacts are caused by the size and shape of fault-zone structures instead of by off-fault viscoplastic parameters
- High-frequency ground motions from elastic impacts are more isotropic and have higher P/S radiated energies

**Correspondence to:**
V. C. Tsai,
victor_tsai@brown.edu

**Citation:**
Tsai, V. C., Hirth, G., Trugman, D. T., & Chu, S. X. (2021). Impact versus frictional earthquake models for high-frequency radiation in complex fault zones. *Journal of Geophysical Research: Solid Earth*, *126*, e2021JB022313. https://doi.org/10.1029/2021JB022313

Received 26 APR 2021
Accepted 18 JUL 2021

**Abstract** Earthquakes occur within complex fault zones containing numerous intersecting fault strands. This complexity poses a computational challenge for rupture models, which typically simplify fault structure to a small number of rough fault surfaces, with all other deformation assumed to be off-fault viscoplastic deformation. In such models, high-frequency ground motions originate solely from frictionally mediated, heterogeneous slip on a small number of potentially rough fault surfaces or from off-fault viscoplastic deformation. Alternative explanations for high-frequency ground motion generation that can account for a larger number of fault surfaces remain difficult to assess. Here, we evaluate the efficacy of a recently proposed stochastic impact model in which high-frequency ground motion is caused by elastic impacts of structures within a complex fault zone. Impacts are envisioned to occur in response to fault motion in the presence of geometrical incompatibilities, which promotes transfer of slip onto different fault strands on timescales mediated by elasticity. We investigate the role of a complex fault zone for high-frequency ground motion by comparing the underlying assumptions and resulting predictions of impact and rough fault frictional models. Relative to rough fault frictional models, impact models are characterized by deformation timescales and corner frequencies that are set by elasticity rather than viscoplasticity, relatively angular rather than smoothly varying fault roughness geometries, high-frequency radiation patterns that are more isotropic, and higher $P/S$ radiated energies. We outline ways to discriminate whether impact or rough fault frictional models are more likely to explain observations of high-frequency ground motions.

**Plain Language Summary** Why are some earthquakes of the same size gentler and some of them more destructive? It is known that earthquakes usually occur in fault zones with many intersecting faults, but most models that attempt to explain the variability in destructiveness assume that earthquakes occur on a single fault surface. Here, we consider how the complex interactions between structures within a fault zone with many fault surfaces may contribute to the damaging jerky ground motions. Collisions between discrete fault blocks are envisioned to occur to allow large-scale sliding that is needed to occur during an earthquake. We find that the nature of ground motions from such collisions depends on the sizes and geometries of the blocks, that the spatial variability in ground motions depends on the orientation of the collisions, and that different waves are excited differently by collisions as compared with the shearing motions typically assumed for earthquakes. We compare the collision model with more standard models of earthquakes and discuss how the predicted differences may be used along with certain earthquake observations to distinguish between the models.

## 1. Introduction

For millennia, humans have felt the ground motions from earthquakes but have had a poor understanding of why the shaking occurred, with mythologies ranging from the movement of subterranean turtles or a giant catfish to Poseidon striking the ground with his trident (Nur, 2008; SCEC, 2014). A major advance in our scientific understanding occurred with the 1906 San Francisco earthquake, when Reid (1910) recognized that earthquakes are caused by the release of elastic stress built up on faults like the San Andreas. In the past century, our understanding of earthquakes has advanced considerably, with the Haskell (1964) and Brune (1970) models demonstrating how sudden initiation and ending of fault slip can cause strong accelerations (Madariaga, 1976), and that heterogeneous slip can lead to additional high-frequency ground motions (Aki, 1967; Frankel, 1991; Mai & Beroza, 2002). This understanding motivated many of the latest state-of-the-art ground motion simulations (e.g., Dunham et al., 2011b; Shi & Day, 2013; Wollherr et al., 2018). Such studies explore

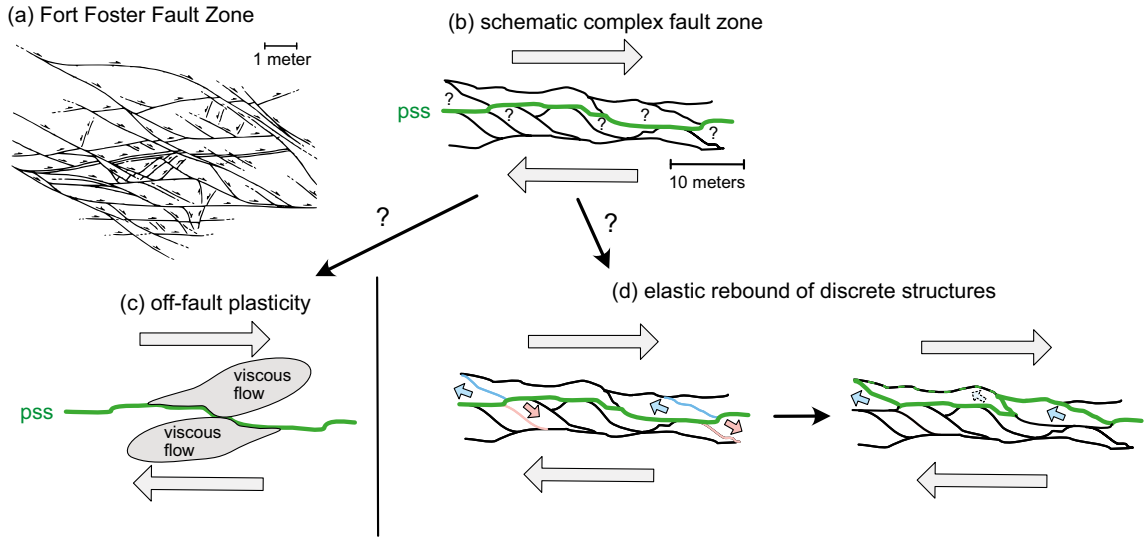


**Figure 1.** Schematic of the physical processes in a complex fault zone. (a) Geometry of the Fort Foster Fault Zone (Maine), which we take as archetypical of a complex fault zone (adapted from Swanson, 1988). (b) Schematic idealized geometry of a complex fault zone with multiple anastomosing fault strands. The green "pss" line denotes the nominal principal slip surface on which fault slip initially occurs. Question marks denote areas of high tensile or compressive stresses induced by the fault roughness during slip. (c) The standard approach to accommodate rough fault slip assumes that when the plastic yield limit is reached off of the main fault, then viscous flow occurs to relieve those stresses. (d) The impact model (Tsai & Hirth, 2020) accommodates rough fault slip by assuming that discrete structures within the fault zone suddenly change their motion (small colored arrows) by transferring slip onto different fault strands (colored fault strands) on timescales mediated by elasticity. The rightmost schematic shows in green the new fault strand with the highest relative slip after slip is transferred onto the blue segments. The blue arrows show the change in motion, which is notably not parallel to the main fault trend and has a component that is fault normal. The dashed green fault strand and dashed arrow show one potential next transfer of slip and impact event.

the possibility that a significant fraction of strong ground motion is facilitated by off-fault viscoplastic deformation that is, in turn, caused by slip on rough faults, with additional complexity caused by wave propagation and scattering through heterogeneous Earth structure (Graves & Pitarka, 2016; Takemura et al., 2009).

Despite the many advances in our understanding of earthquake ground motions, it remains unclear how complex fault zone structure contributes to high-frequency ground motions. There is abundant evidence that fault zones are complex at a range of scales (e.g., Chester & Chester, 1998) including at seismogenic depths (see Figure 1a) (e.g., Faulkner et al., 2003; Swanson, 1988), but even the most complex numerical rupture models typically only have one or a few rough fault segments (e.g., Bruhat et al., 2020; Ulrich et al., 2019), despite the potential importance of these more complex structures in causing significantly stronger high-frequency ground motions. Thus, the current state-of-the-art simulations may still be limited in how accurately they predict high-frequency ground motions, due to computational limitations in the number of fault segments, assumptions made for numerical stability, and the range of physics that is imposed to describe more complex fault-zone interactions.

To better understand how ground motions are affected by complex fault zone structure, such as illustrated in Figure 1a, we provide an in-depth analysis of the ground motion predictions from a stochastic fault-zone structural impact model (Tsai & Hirth, 2020) and contrast the predictions from this model with those from more standard rough single-fault rupture simulations. Specifically, we describe the differences in physical assumptions between the two types of models (Section 2), explain the main quantitative predictions of the impact model (Section 3), and provide an explicit comparison between the two models in a simplified fault-zone geometry for which both models can provide approximate predictions (Section 4).

## 2. Qualitative Comparison of the Elastic Impact Model vs. Rough-Fault Friction Models With Off-Fault Plasticity

Before providing detailed predictions (Sections 3 and 4), we first discuss the qualitative differences specifically between the standard rough fault frictional models and the elastic impact model. The main differences between these two end-member models and some of the reasoning behind why it may be appropriate to

consider an alternative to the rough fault frictional models were described by Tsai and Hirth (2020). A more detailed comparison is presented here to clarify both the context in which we believe the elastic impact model may be appropriate and why current frictional slip simulations may not account for important physical processes that the impact model describes. It is important to keep in mind that the frictional and the impact models are not mutually exclusive; indeed we anticipate that both play an important role for real earthquakes, with frictional slip controlling the low-frequency ground motions, and elastic impacts contributing significantly at high frequencies. A quantitative comparison between the models is presented in Section 4.

### 2.1. Standard Rough Fault Frictional Models With Off-Fault Deformation

The "standard" rough fault frictional models that we compare with are numerical simulations on non-planar faults with rate-and-state dependent friction which include off-fault deformation; we take as archetypical the models of Dunham et al. (2011b), Shi and Day (2013), and Wollherr et al. (2018). While the three numerical simulations mentioned were implemented independently and solved with different techniques, they share many of the same basic physical assumptions, the relevant ones which we describe briefly, and refer the reader to those publications for further details.

In these frictional models, one or a few faults with arbitrary but defined geometries are assumed to slip without fault opening, and with rate-and-state dependent friction (e.g., Rice, 1983) that includes strong rate weakening (e.g., Rice, 2006). Near-planar fault geometries are typically imposed with a given surface roughness that scales in accordance with geologic observations (Dunham et al., 2011b) or to match specific known fault geometries. Three aspects of the models are important to consider for making comparisons to the impact model. First, it is computationally difficult to include more than a few fault surfaces and so multiple connected sub-parallel or anastomosing fault strands are typically not included. Second, for all of the models described, friction is assumed to drop by an order of magnitude from static values for slip velocities in excess of a few tenths of a m/s or slip in excess of tenths of a meter (Rice, 2006). Third, the models all incorporate Drucker-Prager off-fault plasticity with a viscous flow law to accommodate deformation once plastic yield criteria are reached (Dunham et al., 2011a). Within such a numerical framework, including viscous flow is necessary because perfect plasticity results in numerical artifacts and is therefore ill-posed (Dunham et al., 2011a); plasticity is required in rough fault models to relieve the large stresses that would otherwise form around geometrical incompatibilities as slip occurs. As illustrated in numerous studies, off-fault yielding is most prevalent on the extensional side of the fault and on the extensional sides of fault bends (Chester & Chester, 2000; Dunham et al., 2011b; Templeton & Rice, 2008) (see Figure 1c).

There are a number of other earthquake rupture models that are distinct from or modified from the standard rough fault frictional paradigm described above. For example, other studies have examined the role of a low-velocity fault zone (e.g., Huang et al., 2014, 2016), creation of damage during rupture (e.g., Lyakhovsky & Ben-Zion, 2020; Okubo et al., 2019; Xu et al., 2015), and the effects of including off-fault fractures or short branches (e.g., Ma & Elbanna, 2019; Okubo et al., 2019; Ozawa & Ando, 2021). We recognize that these other models include different assumptions (which may or may not include viscoplasticity) and make different predictions from the rough fault frictional models that we compare with the impact model. It is not our intent to discount any of these other possibilities or to suggest that these other physical processes should not be considered. Indeed, some of the physics considered in these other models overlaps somewhat with the physics of the impact model, and future work will be necessary to compare the various specific predictions of these other models.

### 2.2. The Elastic Impact Model of Tsai and Hirth (2020)

#### 2.2.1. Qualitative Description

Here, we discuss the motivation behind, the assumptions of, and some of the qualitative predictions of the elastic impact model of Tsai and Hirth (2020). We expand the discussion to clarify the reasons that we believe the model may approximate realistic fault-zone physics that is currently not accounted for in the standard rough fault frictional models described above. A more detailed quantitative description of the model is presented in Section 3.

The basic question that motivated the elastic impact model can be summarized as follows: How is large-scale earthquake slip accommodated within a geometrically complex fault zone? Numerous geologic observations suggest that most fault zones are complex at the meter to kilometer scale, with many anastomosing fault strands that can mutually cross-cut each other (Chester & Chester, 1998; Faulkner et al., 2003; Rowe et al., 2018; Swanson, 2006; see Figure 1a). Thus, although some fault zones appear to have a single cm-scale principal slip surface (pss; Chester & Chester, 1998; Chester et al., 2004) where slip is dominant (see also the green line in Figure 1b), in many fault zones there are multiple surfaces with significant slip or it is unclear which sub-fault strands have been active during various events (e.g., Rowe & Griffith, 2015). Since such fault zones have meter-scale to kilometer-scale complexity, it is also unclear what physical processes dominate on the scale of this complexity when slip occurs. Specifically, if slip initiates on what is thought to be a rough non-planar pss, what occurs when geometrical incompatibilities start to form during slip? If slip continues along the pss, stresses build up along restraining bends and stresses drop along releasing bends of the fault (see question marks in Figure 1b). With finite slip, Chester and Chester (2000) showed that if the surrounding medium remains perfectly elastic, then many areas especially in extensional regions (i.e., around the releasing bends) would meet a typical plastic failure criterion. The frictional models described above (Section 2.1) account for this by imposing viscous flow where stresses exceed the Drucker-Prager plastic yield limit (Figure 1c).

However, if the fault zone is composed of multiple fault strands, there is another option for accommodating what would otherwise become a geometrical incompatibility, namely, slip can transfer onto adjacent faults such as the blue and red fault segments drawn in Figure 1d (Swanson, 1988, 2006), leading to rearrangement of the discrete structures within the fault zone and without requiring bulk viscous flow or Drucker-Prager yielding. If one considers one of these fault blocks that was initially on one side of the fault but then has slip transferred to its other side, it must then have a change in velocity during the transition that is a substantial fraction of the slip velocity. Although inelastic processes may also occur, the basic physics describing this block's change in velocity is due to elastic compression that increases initially and is then released as the block's velocity changes after slip is transferred. This is the essential physics underlying the elastic impact model of Tsai and Hirth (2020), which was quantified using Hertzian contact theory. Importantly, if friction has minimal control on this process, the direction of impact (momentum change) is determined by the geometry of the local contact surface and can be very different from the large-scale or local slip direction even when the initial velocity is in the slip direction. This dependence on local geometry that may be different from larger-scale fault orientations (e.g., McLaskey & Glaser, 2011) and sudden relaxation of stress concentrations at geometric incompatibilities through elastic rebound makes the impact model different from a model solely of fault slip transfer. However, a number of the predictions of the stochastic impact model are similar to that of a stochastic slip transfer model. We also note that within the elastic impact framework, complex fault zone structure is assumed to exist; the question of what caused the complex structure is not answered but instead is separated from the question that is addressed of how ground motions are affected by the assumed structure.

#### 2.2.2. Questions and Caveats of the Elastic Impact Model

The idealization inherent in the elastic impact model raises a number of issues. First, while the idealized cartoon of this process drawn by Tsai and Hirth (2020) depicts fault blocks as particles that freely impact and rebound as they collide with other structures or the side of the fault zone, all that is required is for momentum to change quickly. Thus, the process of elasticity-mediated momentum transfer described above does not require substantial empty space within the fault zone, (although "implosion breccias" [Sibson, 1986]) observed in natural fault zone structures demonstrate the local creation of some open space during earthquakes, and fault opening also occurs in laboratory shear experiments (Ngo et al., 2012). At times well in advance of impact, as well as times well after impact, the velocity of each block could deviate substantially from a typical impact trajectory, for example, if another impact were to subsequently occur. Thus, even with the high compressive stresses under which most earthquakes occur, the impact physics may be relevant. However, whether the Hertzian contact theory outlined in Tsai and Hirth (2020) is appropriate may be questioned; this point is analyzed in Section 3.1.

Second, if friction remains high (i.e., follows Byerlee's law) along the various faults in question, then there would be some modification to the purely elastic impact due to the frictional forces. Thus, the elastic impact

model is best thought of as an idealization that may be most relevant when the friction coefficient is very low (e.g., below 0.3), such as during an active earthquake rupture, when it is thought that one or more dynamic weakening mechanisms act to dramatically lower friction (e.g., Rice, 2006; Tullis, 2015), as described in Section 2.1. In this context, it is noteworthy that pseudotachylite (resulting in low dynamic friction) is observed along many of the interacting faults segments, including the complex natural fault geometries noted above (e.g., Rowe et al., 2018; Swanson, 1988).

Third, given that one of the elastic impact model's primary predictions is related to the timescale of elastic impact, there is an important question about whether the elastic contact time is what sets the timescale for the momentum transfer, or if other processes are important. For example, processes related to yielding may play a role in the timescale of "impact," and even if yielding is instantaneous, the loading phase of the elastic "impact" may occur over a longer timescale than the unloading phase, unlike in the free collision case where the loading/unloading phases are equal. While we acknowledge these possibilities, we nonetheless believe it is worthwhile to evaluate the prediction from a purely elastic impact model, even if reality is likely to depart somewhat from this idealized scenario. If predictions made from the elastic impact model agree with observations, then that is the reason to use it; conversely, if the predictions disagree with observations then the model can be falsified or additional complexity should be considered.

Finally, while the previous discussion considers just a single momentum transfer event, it is likely that as fault slip continues, many such events occur, which we treat as multiple impacts. This process is somewhat analogous to the occurrence of acoustic emissions in analog laboratory experiments without localized slip surfaces (e.g., Bolton et al., 2020), where smaller microslip events exhibit a complex spatiotemporal evolution preceding and during the larger, system-sized events (Trugman et al., 2020), and result in significantly non-double couple mechanisms (Kwiatek et al., 2014). Since stress is transferred to different structures during each microslip cycle, the process may also be thought of as related to the dynamic creation and destruction of force chains across the fault zone. While force chains are usually thought of as being quasistatic, with force chain lifetimes being much longer than the elastic contact time (e.g., Campbell, 2003; Tordesillas, 2007), the timescale over which stresses are transferred may still be related to the elastic contact time even in the quasistatic limit. Furthermore, during an earthquake when ~m/s slip rates are much higher than in typical force-chain laboratory experiments (e.g., Daniels & Hayman, 2008), the lifetime of force chains may be more commensurate with timescales related to elastic contact theory.

## 3. Quantitative Predictions of the Elastic Impact Model

Since some of the quantitative predictions of the elastic impact model remain unclear, here, we provide a more complete analysis of the model described by Tsai and Hirth (2020).

### 3.1. Hertzian Contact vs. Mated Contact

We first discuss the question of whether the Hertzian contact theory assumed by Tsai and Hirth (2020) is the appropriate mathematical framework for the conceptual model of elasticity-mediated momentum transfer described in Section 2.2. The Hertzian contact theory assumed in Tsai and Hirth (2020) describes the force and associated deformation between two elastic particles initially not in contact and with initial relative velocity $V_z$ directed toward each other (see Figure 2a), which subsequently contact and then rebound. The timescale of such a contact is:

$$T_c \approx 2.9\left(\frac{m^2}{RE_*^2V_z}\right)^{1/5} \approx 2.9\left(\frac{16\pi^2\rho^2\xi^4}{9E_*^2V_z}\right)^{1/5} R \approx 0.014\frac{\mathrm{s}}{\mathrm{m}}\cdot R \quad (1)$$

where $m$ is the mass of the particle, $R$ is the effective radius of curvature, $E_* = E/\left[2\left(1-\nu^2\right)\right]$, $E$ is the Young's modulus, $\nu$ is the Poisson's ratio, $V_z$ is the impact speed, $\rho$ the is particle density, and the second approximation assumes an ellipsoidal impactor with aspect ratio $\xi > 1$ impacting a flat surface. If the contact is already loaded (e.g., at the initiation of earthquake rupture), only the rebound occurs, and over a times-

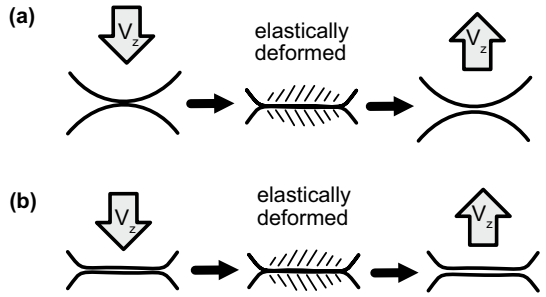


**Figure 2.** Schematic of (a) Hertzian elastic contact vs. (b) mated elastic contact for an initial relative velocity of $V_z$. The hatched region denotes the area with significant elastic deformation.

cale that is exactly one half of $T_c$. Tsai and Hirth (2020) also noted that Hertzian contact theory for such a model also implies that the force time history is nearly a truncated sinusoid, with force time history equal to:

$$\vec{i}\left(t\right) = \vec{A}\cos\left(\frac{\pi t}{T_c}\right)\cdot \mathrm{rect}_{T_c}\left(t\right) \tag{2}$$

where rect is a unit boxcar function, and the amplitude $A$ is such that the impulse is equal to:

$$\int_{T_c}\vec{i}\left(t\right)dt = \left(1+e\right)m\Delta\vec{w} \tag{3}$$

where $e$ is the coefficient of restitution, $m$ is the mass of the particle/structure, and $\Delta\vec{w}$ is the initial relative velocity.

An alternative quantitative model for the same conceptual model is what one could call "mated" elastic contact and impact, where the initial contact begins with a large area of nominal contact and deformation continues primarily over this same area (see Figure 2b). This situation could arise, for example, if the surfaces of the two particles initially were closely mated together even when not elastically stressed.

To a first approximation, the equations governing mated impact are simpler than that of Hertzian impact, since the area of contact and hence elastically deforming region remains approximately the same throughout the impact process. If one assumes the elastically deforming region is unchanged throughout, then there is an exact analog with the standard elementary physics problem of a projectile mass that encounters a spring at an initial velocity of $V_z$ and subsequently rebounds with the opposite velocity. The spring constant for this case is given by $k = E_k R$ where $E_k = E$ (Young's modulus) if the deformation is primarily axial or $E_k = G$ (where $G$ is the shear modulus) if deformation is primarily in shear, and $R$ is the length scale over which this deformation occurs. The way Figure 2b is drawn, $E_k \approx E$ and $R$ is the radius of an approximately spherically shaped particle. However, one could imagine one of the fault block structures in Figure 1 impacting another block in a manner where there is primarily shear deformation so that $E_k \approx G$ or in which the aspect ratio $\xi$ is large. With these assumptions, the timescale of elastic contact is:

$$T_c = \sqrt{\frac{m}{k}} \approx \left(\frac{m}{E_k R}\right)^{1/2} \approx \left(\frac{4\pi\rho\xi^2}{3E_k}\right)^{1/2} R \approx 0.0026\frac{\mathrm{s}}{\mathrm{m}}\cdot R \tag{4}$$

if we choose nominal values as before, and $\xi = 5$ and $E_k = G$. Importantly, the scaling of Equation 4 is very similar to that of Equation 1, being linear in $R$, and strictly independent of $V_z$ (Equation 1 is weakly dependent on $V_z$), and scaling with $\xi$ to a positive power. Both impact models predict contact times and therefore forcing timescales that increase linearly with structure size, $R$, but with different scaling factors. Numerically, with realistic parameters, the scaling factor for Equation 4 is about one order of magnitude smaller than in Equation 1, suggesting that the size of structures to create the same timescale of impact would be an order of magnitude larger than the size estimated with Equation 1. For example, to achieve a corner frequency of 20 Hz, Equation 4 with the nominal values from above would predict a particle size of 19 m instead of 3.6 m. Finally, in this elementary spring-projectile case, the force time history is exactly a truncated sinusoid, with force time history proportional to $i\left(t\right) = \cos\left(\pi t\ /\ T_c\right)\cdot \mathrm{rect}_{T_c}\left(t\right)$, so that the spectrum is exactly an omega squared spectrum, similar to as in the Hertzian case (Equation 2). Perhaps unexpectedly, the mated impact timescale scales in a similar manner to the timescale of rupture over a patch of size $R$ since rupture speed scales with elastic wave speed, and elastic wave speed is the relevant speed for purely elastic deformation. Unfortunately, this makes mated impact more difficult to distinguish from rupture over the same (small) area, though the physical deformations and orientations of these deformations are different.

It is not obvious which of the two models of Hertzian contact (Equation 1) vs. mated contact (Equation 4) is most appropriate for the impact of structures within a rupturing fault zone during an earthquake. Static faults are under significant confining stresses, which suggests that mated contacts may be more likely. However, geologic observations suggest that small amounts of opening and closing within fault zones occur during dynamic fault slip (Brune, 2001; Kwiatek & Ben-Zion, 2013; Mitchell et al., 2011; Rempe et al., 2013).

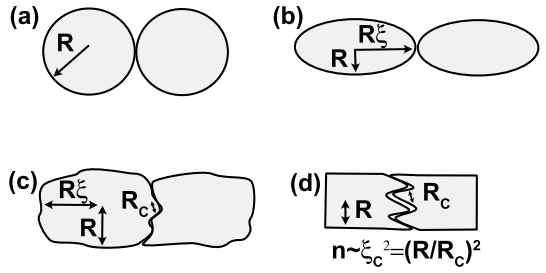


**Figure 3.** Schematic of particle contacts for different assumed geometries. (a) Spherical contact, (b) Elliptical contact, (c) Three length scales, (d) Number of contacts.

Thus, particularly during the highest slip rate portions of earthquake rupture, when significant rearrangement of structures is ongoing, Hertzian contact theory may be more appropriate than mated contact for describing the timescale of impacts. Understanding the distribution of structure sizes and the rheologic properties of the fault blocks and intervening fault surfaces is also critical for predicting which contact geometry is more appropriate. For example, if the most relevant large structures for producing ground motion are bounded by a relatively weak hydrothermal breccia, fault gouge, or frictional melt that is significantly weaker than the larger block then one would expect Hertzian contact to be a better description. In contrast, if the large structures are closely surrounded only by other geometrically mated structures with similar rheological properties then one might expect the mated contact description to be more appropriate. Given the range of possible geometries and bounding rheologies between structures, and the lack of definitive observations, it is prudent to remain agnostic regarding the answer to this question and we accept the order-of-magnitude uncertainty in predicted sizes. Fortunately, since the two contact models predict a similar scaling with the important physical properties, most importantly the same scaling of contact times with the average size of the particles and near independence of contact time on the impact velocity, the generic behavior of the two models is very similar. Thus, the agnostic choice is not overly restrictive relative to the predictions of the model framework.

### 3.2. Contact Time for Geometrically Complex Structures

As mentioned briefly by Tsai and Hirth (2020), real fault zone structures are likely significantly more complex than the simple spherical (see Figure 3a) or ellipsoidal shapes (Figure 3b) used to calculate the contact time in Equations 1 and 4. In reality, both geometrical models should have at least three different length scales of importance: the particle width $R$, the particle length $\xi R$, and the contact-scale radius of curvature which we denote $R_C$, where Tsai and Hirth (2020) assumed $R_C$ was equal to $R$ for simplicity (see Figure 3c). Moreover, the number of effective points of contact, $n$, is expected to vary significantly between different geometrical shapes and depends on the particle roughness, which in turn is related to the contact aspect ratio $\xi_C = R/R_C$ (see Figure 3d). For real fault zones, we expect particles to be in close proximity to their neighbors so that in both models, one may expect $n$ to increase as $R_C$ decreases (or as $\xi_C$ increases). More specifically, $n$ may be related to the total area available for contact ($R^2$) divided by the area of each elastic deformation ($R_C^2$) so that we may expect $n \approx \xi_C^2$. Large $n$ reduces the effective mass, reducing $T_C$, which more than offsets the increased $T_C$ due to the smaller $R_C$ for both models. With the above assumptions, the modified timescale for the Hertzian model is $T_c \approx 2.9\left(16\pi^2\rho^2\xi^4 / 9E_*^2V_z\xi_C\right)^{1/5} R$ and for the mated contact model, $T_c \approx \left(4\pi\rho\xi^2 / 3E_k\xi_C\right)^{1/2} R$. In both cases, accounting for this additional particle roughness decreases the estimate of $T_C$, though only by a modest amount in the Hertzian case. Observations of high-frequency earthquake spectra for fault zones with very detailed constraints may be used to distinguish between the impact timescale predictions and those of more traditional models where the spectra are instead related to stress drop (Abercrombie, 2021; Allmann & Shearer, 2009).

### 3.3. Predicted Forcing for a Distribution of Particles

As discussed by Tsai and Hirth (2020), for a complex fault zone with many fault blocks within the fault zone, one would expect many momentum change events that we call elastic impacts, and the ground motion from the elastic impact model would have contributions from each impact force. In other words, if there are $N$ momentum change events, the forcing time series is assumed to be:

$$F(t) = \sum_{k=1}^{N} \vec{i}\left(t - \Delta t_k\right) \tag{5}$$

where $\vec{i}(t)$ is given by Equation 2, $\Delta t_k$ are the times of each impact event, and $T_c$ is given by either Equations 1 or 4. This description applies to the case where the radiation results from the force of each impact

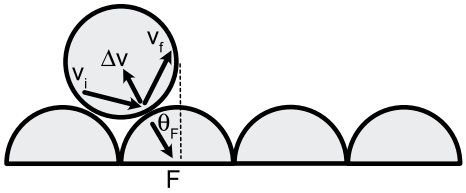


**Figure 4.** Schematic of accessible impact angles. $V_i$ represents the initial velocity and $\Delta \boldsymbol{V}$ shows the direction of the momentum change due to the geometry of contact.

of each block against an adjacent block. By applying this description, we implicitly assume that the impacting block is freely slipping with respect to the bulk Earth, and conversely that the impacted block is instantaneously coupled with the surrounding medium—so that ground motion is radiated. It is the mass $m$ and relative velocity $\Delta\vec{w}$ of the freely slipping first block that should be used to calculate $\vec{i}\left(t\right)$ here.

The orientation of the impact forces depends both on the orientation of the many blocks as well as on the relative velocities of the blocks immediately prior to the interaction. As discussed in more detail in Farin et al. (2019), if it is assumed that the orientation of each of the particle impacts is related only to the local geometry of contact, then a statistically averaged effective root-mean-square (RMS) forcing in each direction can be calculated by summing the square of the individual force contributions on a distribution of surface orientations. This approach assumes that every impact is statistically independent of all other impacts and, for example, assumes that any reactionary forces needed to conserve momentum or angular momentum are still uncorrelated in time (and thus do not cause the forcing to result in a moment tensor or dipole source). In order for the reaction force to radiate waves independently, the time between successive interactions of any given particle must be a significant fraction of the impact time and uncorrelated in phase.

While the contact geometry of structures within any particular fault zone may be somewhat unique and impossible to evaluate without detailed observations of that fault zone, there are approximations one can make to estimate the magnitude and direction of the RMS force in a complex fault zone. Following Farin et al. (2019), we assume that the particles within a complex, rough fault zone are driven by the large-scale shear velocity $V_S$ of one side of the fault zone relative to the other. Given fault zone roughness length scales that are a significant fraction of the particle sizes, Farin et al. (2019) found that the instantaneous deviation in velocity of any given particle from the steady-state shear velocity (i.e., earthquake slip velocity) is expected to be a large fraction of the slip velocity. In this situation, the relative velocities have fluctuations in all directions and the simplest assumption is that the magnitude of fluctuation is also the same in all directions, despite the strong directionality of the shear forcing. With this approximation, the RMS impulse from many elastic impacts can be calculated by integrating over the accessible range of solid angles available based on the geometry of contact, as described in Appendix A of Farin et al. (2019) (see Figure 4). Although particle shapes may be quite complicated, the simplest assumption would be that all angles are equally accessible, in which case the forcing is completely isotropic, with

$$I_{x,\mathrm{RMS}} = I_{y,\mathrm{RMS}} = I_{z,\mathrm{RMS}} = \frac{1}{3}\left(1+e\right)mV_S\sqrt{N} \tag{6}$$

where $e$ is the coefficient of restitution, $m$ is the particle mass, and $N$ is the number of impacts. While Farin et al. (2019) found that there can be a significant geometrical bias toward boundary-normal impact for the scenario of spherical particles impacting a boundary composed of half-spherical particles (see Figure 4), this bias only arises in the unrealistic repeating pattern case. In contrast, taking the orientations of all subfaults in Figure 1a as representative of the possible impact angles in a realistic fault zone, we find (by integration over all surfaces) that the distribution of predicted forcing angles is within ~5% of the completely isotropic case. We return to the question of the isotropy of ground motion in the next section.

### 3.4. Predicted Radiation for a Distribution of Particles

Once the forcing or impulse functions are determined (Section 3.3), the predicted ground motions are calculated by convolution with the point-force Green's function $G_{jk}(t)$. For a realistic structure, the Green's function can be very complicated and in general should be evaluated numerically for a known velocity structure. However, to get a sense of the predicted radiation and radiation pattern from the impact model, we can use a homogeneous far-field Green's function. With this assumption, the far-field $P$-wave radiation in the $i$ direction for a point force in the $j$ direction is given by:

$$u_i^P = \frac{1}{4\pi\rho\alpha^2}\gamma_i\gamma_j\frac{1}{r}F\left(t-\frac{r}{\alpha}\right) \tag{7}$$

where $\gamma_i$ are the direction cosines, $r$ is the distance to the source, $F(t)$ is the forcing time series, and $\alpha$ is the $P$ wave speed (Lay & Wallace, 1995). Defining $\theta$ as the angle to the forcing direction, then the radiation pattern has a simple cos$\theta$ pattern, or $\cos^2\theta$ pattern for the squared ground motion. Similarly, for far-field $S$-wave radiation:

$$u_i^S = \frac{1}{4\pi\rho\beta^2}\left(\delta_{ij} - \gamma_i\gamma_j\right)\frac{1}{r}F\left(t - \frac{r}{\beta}\right) \tag{8}$$

where $\beta$ is the shear wave speed. Again, the radiation pattern has a simple $-\sin\theta$ pattern or $\sin^2\theta$ pattern for the squared ground motion.

If the stochastic forcing is isotropic, then the radiated ground motions are also isotropic for both the $P$ and $S$ waves, since one would average the single force radiation patterns equally over the entire sphere. Alternatively, if the strength of forcing is different in different directions (potentially because only certain angles are accessible) then solid angle integration must be done to calculate the effective ground motion radiation pattern. If the angle to fault normal is given by $\theta_F$, the azimuthal angle is $\phi_F$, and the relative strength of forcing is $S_F\left(\theta_F,\phi_F\right)$ then the average squared $P$-wave radiation pattern is given by:

$$\langle\left(\gamma_i\gamma_j\right)^2\rangle = \frac{\int_0^{\pi}\int_0^{2\pi} S_F \sin\theta_F \cos^2\psi\, d\phi_F d\theta_F}{\int_0^{\theta_{F0}}\int_0^{2\pi}\sin\theta_F d\phi_F d\theta_F} \tag{9}$$

and the average squared $S$-wave radiation pattern is given by:

$$\langle\left(\delta_{ij} - \gamma_i\gamma_j\right)^2\rangle = \frac{\int_0^{\pi}\int_0^{2\pi} S_F \sin\theta_F \sin^2\psi\, d\phi_F d\theta_F}{\int_0^{\theta_{F0}}\int_0^{2\pi}\sin\theta_F d\phi_F d\theta_F} \tag{10}$$

where $\cos\psi = \cos\theta_F\cos\theta + \sin\theta_F\sin\theta\cos\left(\phi - \phi_F\right)$, where $\left(\theta,\phi\right)$ are the directional coordinates of the station, and $\left(\theta_F,\phi_F\right)$ are the directional coordinates of the forcing relative to the fault normal. With realistically shaped structures within a realistic fault zone, the half-spherical assumption of Figure 4 (as suggested by Tsai and Hirth 2020) is almost certainly too idealized and we believe it a better assumption that all impact directions are equally likely given the complex geometries within a fault zone (see e.g., Figure 1a) and the fact that there may not be symmetries within a real fault zone. Thus, we predict nominally isotropic RMS radiation patterns from a stochastic sets of impacts. We note that even when the impact force directions are somewhat limited, like with the limited fault orientations in Figure 1b, the average RMS radiation pattern is still relatively isotropic, for example, within 20% of purely isotropic in the case of Figure 1b. One could potentially relax the isotropic assumption if there were sufficiently good constraints on the local orientation of impact contacts to warrant it.

### 3.5. Radiated Energy

The radiation from the impact model is in the form of the sum of many independent single forces (Equations 7 and 8), rather than as a sum of moment tensor sources, as in standard frictional models. This difference leads to different scaling of the ratio of $S$-wave to $P$-wave energy. $P$-wave displacement radiation from a moment tensor is given by:

$$u_i^P = \frac{1}{4\pi\rho\alpha^3}\gamma_i\gamma_p\gamma_q\frac{1}{r}\dot{M}_{pq}\left(t - \frac{r}{\alpha}\right) \tag{11}$$

and $S$ wave radiation from a moment tensor is given by:

$$u_i^S = \frac{1}{4\pi\rho\beta^3}\left(\delta_{ip} - \gamma_i\gamma_p\right)\gamma_q\frac{1}{r}\dot{M}_{pq}\left(t - \frac{r}{\beta}\right) \tag{12}$$

In general, total radiated energy is proportional to $V\omega^2u^2$ where $V$ is the wave speed, $\omega$ is frequency and $u$ is the particle displacement amplitude. Thus, the radiated $P$ energy for a moment tensor is proportional to $\alpha^{-5}$, and radiated $S$ energy for a moment tensor is proportional to $\beta^{-5}$. In contrast, the radiated $P$ and $S$ energies for a single force are proportional to $\alpha^{-3}$ and $\beta^{-3}$ respectively (Lay & Wallace, 1995). Thus, the $S/P$ energy ratio for moment tensor sources is $(\alpha/\beta)^5$ whereas the $S/P$ energy ratio for single forces is $(\alpha/\beta)^3$. Since the

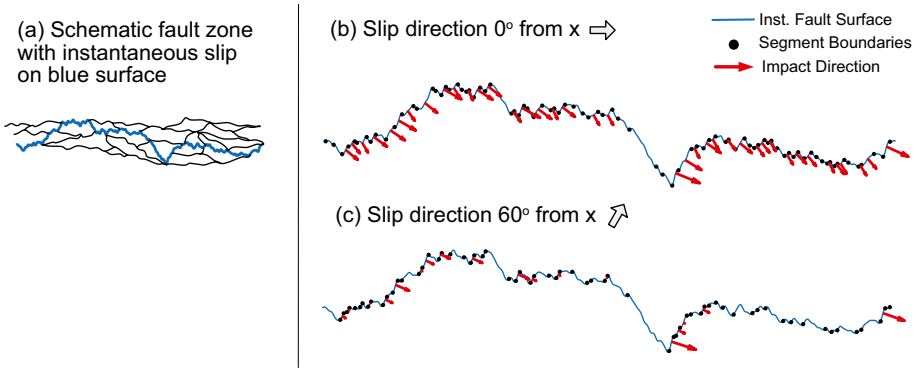


**Figure 5.** (a) Example schematic fault zone with instantaneous principal slip surface (blue line). (b and c) Instantaneous fault surface (blue line) with impact site segment boundaries denoted (black circles), and impact direction with magnitude scaled by $\overline{\theta}_R$ (red arrows). Directions are shown for pure right lateral slip and impact of upper surface onto lower surface. Impacts of lower surface onto upper surface are just as likely. (b) Slip direction aligned with $\hat{x}$. This example has 39 impact sites. (c) Slip direction 60° counterclockwise of $\hat{x}$. This example has 18 impact sites. Segment boundaries are points where overlap from slip approaches zero.

impact model is composed of a sum of single forces, the $S/P$ energy ratio for the impact model is also predicted to be $(\alpha/\beta)^3$. When the effects of scattering are accounted for and/or minimal, measuring the energy ratio would therefore be diagnostic of whether single forces like impacts are present and therefore which of the two models is appropriate.

### 3.6. Estimated Number of Impacts

So far, we have focused on the predicted forces for a single impact and the expected radiated energy from a collection of impacts, but we have not yet made an estimate of the number of impacts that may be expected during any given earthquake. To make such an estimate, we posit that for any instant during the earthquake, slip can be focused on one or multiple slip surfaces. For example, in Figure 1c, one can think of tracking the "pss" (green line labeled pss) with time as impacts occur and lead to transfer of slip between the various possible slip surfaces. Given an instantaneous pss and the direction of local relative slip everywhere along this surface (which is not necessarily in the direction of large-scale fault motion), one can estimate the amount of slip necessary to produce another structural change in the pss (i.e., an impact) based on when the stress built up on a nominal new impact point would reach a yield stress (see Figure 5). Taking the most important structure size, $R = R_{73}$, that is the 73rd percentile of the structural size distribution (which is larger than the median size due to the stochastic addition of Equation 5) (Tsai & Hirth, 2020), we estimate the stress built up for a slip of $S$ as:

$$\sigma \approx \frac{E\overline{\theta}_R S}{R} \tag{13}$$

where $\overline{\theta}_R$ is the average angle (in radians) between the local slip surface and the local slip direction, averaged over a length scale of $R$. Accounting for $\overline{\theta}_R$ partitions the possible strain ($\sim S/R$) into the component that cannot be released by fault motion. For a perfectly planar fault surface, $\overline{\theta}_R = 0$ so that no elastic stresses build up. In contrast, if $\overline{\theta}_R \sim 1$ then each unit of slip results in a strain related to that unit slip. One can then compute when this stress exceeds a yield stress $\sigma_{\text{yield}}$. For example, using $E = 5 \times 10^{10}$ Pa and $\sigma_{\text{yield}} = 100$ MPa, then an impact is expected at $S/R \sim 2 \times 10^{-3}$ for $\overline{\theta}_R \sim 1$ or $S/R \sim 2 \times 10^{-2}$ for $\overline{\theta}_R \sim 0.1$. Thus, for $R = 50$ m, which Tsai and Hirth (2020) nominally estimated might be appropriate for an earthquake of moment $10^{16}$ Nm, with an average total slip in the ~0.3 m range (Mai & Beroza, 2002), that would imply $S \sim 0.1$ m for $\overline{\theta}_R \sim 1$ or $S \sim 1$ m for $\overline{\theta}_R \sim 0.1$. This in turn would mean approximately three impacts at each site over the full slip of the event in the former case, or ~0.3 impacts per site in the latter case. The total number of impacts over the event would then be obtained by multiplying this number by the number of such points on a pss. Given arbitrary complexity, the number of such points could in theory be quite large. For example,

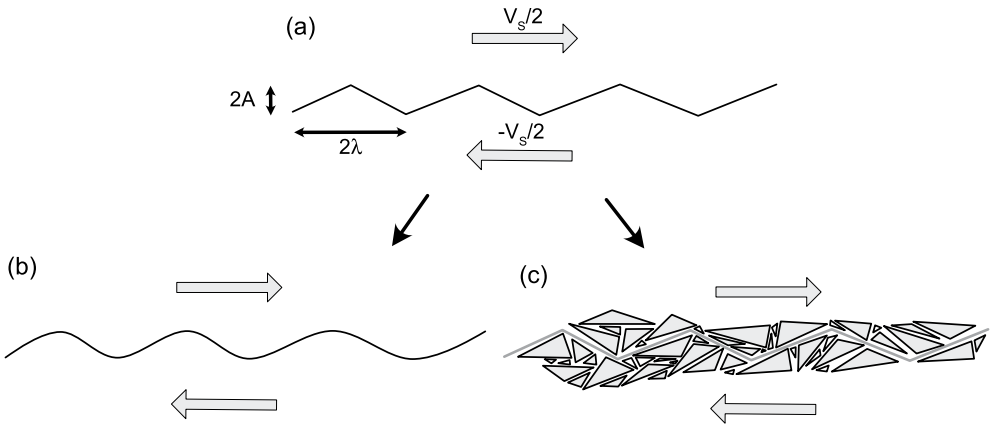


**Figure 6.** (a) Schematic of a sawtooth fault with imposed slip velocity $V_S$. (b) Sinusoidal approximation, (c) Particle approximation.

at one extreme, if every 50 m segment had an intersecting fault strand with $\overline{\theta}_R \sim 1$, then the full fault of area (~10 km$^2$) could have up to 4,000 sites, implying a total of 12,000 impacts during the event. However, a smoother fault of the same area with $\overline{\theta}_R \sim 1$ occurring only every 200 m would have 250 sites and thus 750 total impacts in this scenario. The average rate of impacts would be the total number of impacts divided by the earthquake duration. Two examples of the impact sites, impact directions and $\overline{\theta}_R$ for pure right lateral slip on a given pss are shown in Figure 5. While the impact directions for the unidirectional slip in Figure 5 is not isotropically distributed, the expected partition of slip onto many different structures in different directions would cause the combined impacts to be nearly isotropic (see Sections 3.3 and 3.4).

## 4. Quantitative Comparisons of the Elastic Impact Model With Rough Fault Friction Models

To quantitatively compare the predictions from the rough fault frictional models of Section 2.1 with those from the elastic impact model of Section 2.2, we idealize predictions for the simplest scenario in which predictions from both models are possible. Making such a comparison is not straightforward since the assumptions and setup of the two models are inherently different. Furthermore, because the predictions of the elastic impact model are only potentially dominant at high frequencies and should be superimposed on a more standard system-scale (i.e., planar) fault model for the full ground motions, we make predictions for the case of constant slip rate across the fault zone for which the ground motion due to large-scale acceleration is zero. The rupture tip is therefore assumed to be sufficiently far ahead of the zone for which forcings from the two models are calculated, and in this scenario, there are no other sources of heterogeneity in large-scale slip which would otherwise contribute additional differences to the predictions. This simplification allows us to concentrate on the essential differences in predictions between the standard rough fault frictional model and the elastic impact model without incorporating the physics of a dynamic rupture. We further simplify to the scenario of a fault with perfectly periodic sawtooth roughness (see Figure 6a).

Even with these simplifications, neither model can be evaluated strictly within this setup, for different reasons. For the rough fault frictional model, the sawtooth pattern of the assumed fault is incompatible with assumptions for how stresses are modified by fault roughness. Specifically, due to the discontinuities in the derivatives of the assumed fault profile, the predicted stresses on the fault would be infinite since it is along-fault gradients of these derivatives that are used to compute stresses (Chester & Chester, 2000). The infinite on-fault stresses cannot be reduced without modifying the fault geometry. This problem raises an important issue with regards to how realistic faults with sharp discontinuities can be effectively modeled within any numerical framework. However, the sawtooth fault can be approximated as a sinusoidal fault with the same roughness (see Figure 6b). While it is unclear how this approximation affects the predictions, evaluating the sawtooth fault within the frictional framework is beyond the scope of this work. However, due to the

importance of understanding real faults with angular intersections, we suggest it would be worthwhile for the community to further consider how to address this issue.

For the elastic impact model, evaluating predictions for the sawtooth fault has the complication related to the fact that there is a single fault surface. By construction, the elastic impact model requires a fault zone with a distribution of discrete structures (particles), and a prediction cannot be made for a single fault surface of any geometry since there are no defined structures that can undergo an impact as described in Section 2.2. To evaluate the elastic impact model, then, we assume that the sawtoothed main fault (pss) is surrounded by a large number of cross-cutting faults that breaks the fault zone into discrete structures (see Figure 6c). To make a stochastic ground motion prediction, the distribution of structure sizes is assumed to be known, and the distribution of impact angles is assumed to be known. If a completely deterministic prediction is desired, the specific timing of each impact (strength and direction and size of contact) would need to be known. Although this type of information can be extracted from exhumed fault zones (e.g., Figure 1a), it is very unlikely to be knowable for any active fault application, but may be useful to think about to gain a conceptual quantitative understanding of what is predicted, and we show an example of this below.

### 4.1. Viscoplastic Off-Fault Deformation Ground Motion Prediction

The predictions for the stresses caused by fault slip on an idealized sinusoidal fault have been calculated following the approach of Chester and Chester (2000); here, we evaluate the additional contribution to the ground motion that is predicted by the off-fault viscoplastic deformation. Chester and Chester (2000) determined the locations where viscoplastic deformation is expected, and Figure 7 shows one wavelength of the fault along with the predictions for principal stress directions given slip along the sinusoidal fault (blue/red stress directions are equivalent to those plotted by Chester & Chester, 2000 in their Figure 3) and for the failure region (black line in Figure 7). To determine the additional ground motions produced by distributed viscoplastic failure (which occur independently of any ground motion caused by dynamical feedbacks creating heterogeneous slip that might be promoted by the effects of viscoplastic failure, which we do not include here), it remains to integrate the predicted stress glut resulting from these stresses over the failure volume to obtain the average predicted moment tensor (Backus & Mulcahy, 1976; Dahlen & Tromp, 1998). Predicted ground motions can then be calculated in the same way in which ground motions from moment tensors are usually calculated. The integration is straightforward because the instantaneous stress glut rate is proportional to the known elastic stresses over the failure region and zero outside the failure region, and moment rate is equal to stress glut rate giving:

$$\dot{M}_{ij}^{viscoplastic} = \frac{E}{\eta} \int_{failure} \sigma_{ij} dV \tag{14}$$

where $E/\eta$ is the ratio of the respective elastic modulus and viscosity for each component of stress (which for simplicity here is assumed constant). As an approximation, we assume the total viscoplastic moment contribution is dominated by the early stages of failure, or alternatively that the effective viscosity is low such that the change in $\sigma_{ij}$ is small:

$$M_{ij}^{viscoplastic} = \frac{E\Delta t}{\eta} \int_{failure} \sigma_{ij} dV \tag{15}$$

where $\Delta t$ is the duration of significant viscoplastic deformation. The resulting moment tensor is shown in Figure 7. The contributions from the other side of the fault are identical, due to symmetry, and there is a contribution from each releasing bend along the fault. The total magnitude of the contribution thus depends on the integrated time that the stresses remain above the assumed plastic failure strength, viscosity, and also the length of the fault. While the mechanism is determined by $\sigma_{ij}$, the magnitude or moment and frequency content depends significantly on the assumed viscosity, since this determines both how long the region remains in plastic failure and how much total stress glut there is.

We can calculate an upper bound on the amplitude of the moment tensor contribution, which is the contribution that would occur if the stresses were to reduce to zero within the failure region over the course of the

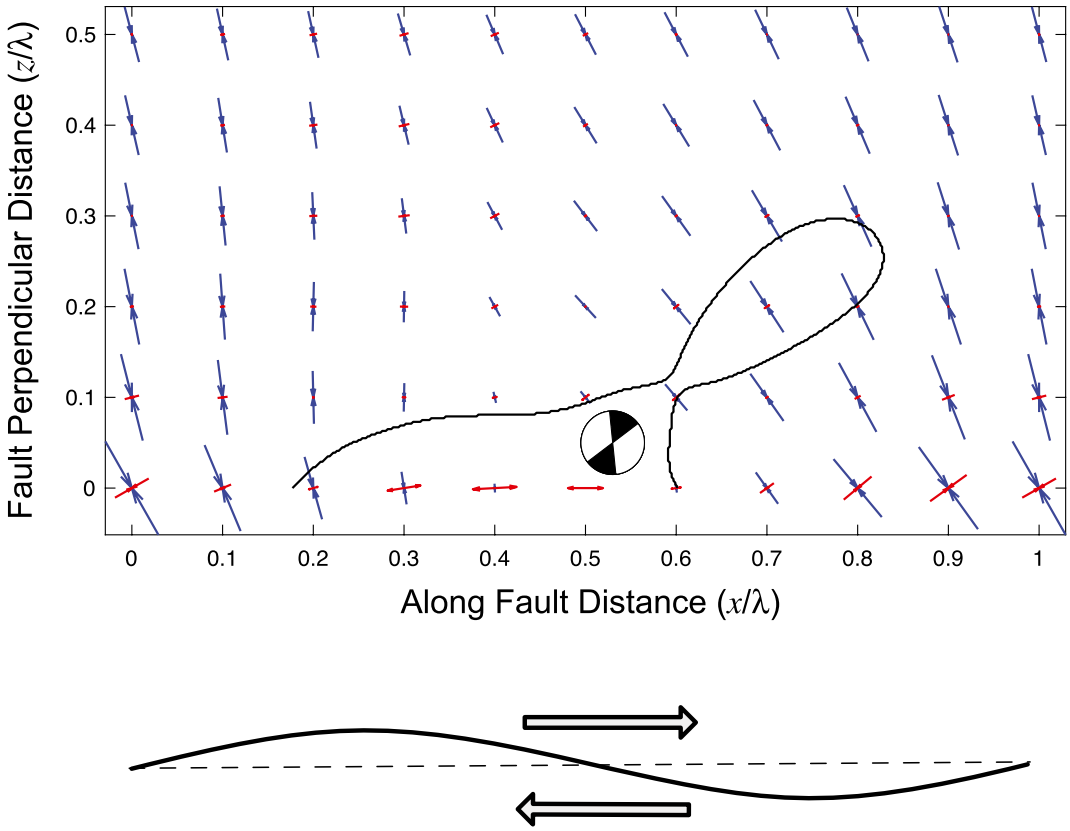


**Figure 7.** Example stress field caused by slip on a sinusoidal fault (bottom), with $\mu = 0.325$, $\theta_\sigma = 70°$, $\bar{\sigma}_{zz} = 100$ MPa, $T_0 = 20$ MPa, $\tau_0 = 190$ MPa, $\mu_* = 0.6$ (see Chester & Chester, 2000). Blue arrows denote the largest compressive stress, red arrows denote the smallest compressive (or tensional) stress. The area encompassed by the black line is the area where viscoplastic yielding is predicted. The focal mechanism represents the predicted contribution of the viscoplastic yielding to the ground motion. The calculated normalized moment tensor principal components are −1, 0, 0.3137.

earthquake. For the moment tensor in Figure 7, the upper bounds on the principal components are −8.2%, 0%, and +2.6% of the total moment available when slip is *L/2* and with other parameters as in Figure 7. As shown, this moment tensor's orientation is misaligned with that of the double-couple fault orientation, and has a significant non-double couple mechanism that includes an implosive component and thus radiates some component of its energy isotropically. Decomposing the moment tensor into a pure double couple part and an isotropic part, the double couple moment is approximately 1.9 times the isotropic moment, even without accounting for the potentially much larger double couple component from slip on the main fault.

The timescale and hence the frequency content of the radiation from off-fault deformation in this model is strongly dependent on the assumed viscosity. With assumed viscosities low enough that failure instantaneously keeps pace with yielding, the timescale at which the deformation occurs is that of the creation of stresses above the yield stress. For high assumed viscosities, the timescale is comparable to the viscoplastic relaxation (Maxwell) time, that is the ratio of the elastic modulus to the viscosity. In these scenarios, then, the assumed viscosity dictates the frequency content of the predicted ground motions. Thus, part of the predicted frequency content is a direct outgrowth of the assumed viscosity. For example, for numerical stability reasons, Dunham et al. (2011b) assume a viscoplastic relaxation time of $\frac{\eta}{E} \sim 8.7 \times 10^{-3}$ s (i.e., $\eta = 278$ MPa · s), which sets a limit on the frequency content of the ground motion with an effective corner frequency at ∼115 Hz (the inverse of the relaxation time). Thus, as Dunham et al. (2011a) acknowledge, an important question of this model is whether the choice of $\eta$ is physically justified and whether the predicted corner frequency is physically constrained. We note that such simulations also have additional main-fault slip heterogeneity that results from the viscoplastic deformation; these slip heterogeneities contribute additional radiation that may be at different frequencies than the ones discussed.

### 4.2. Elastic Impact Ground Motion Prediction

Predictions for the ground motion of the elastic impact model follow Equation 5 with timescales $T_c$ given by Equation 1 or 4 and amplitudes given by Equation 3. In addition, to satisfy momentum and angular momentum conservation, we require additional constraints on the forcing time series that the net integrated force and net integrated torque be zero, so:

$$\int \vec{F}(t)\,dt = 0 \tag{16}$$

and

$$\int \vec{x} \cdot F(t,\vec{x})\,dt = 0 \tag{17}$$

where $\vec{x}$ is the location of the various forces. If locations within the fault zone are too close to spatially resolve, then all the forces in Equation 5 can be assumed to be collocated, Equation 17 is trivially satisfied, and only momentum conservation (Equation 16) needs to be accounted for.

If the orientations, amplitudes, and timings of all the impact forces are known, then the far-field radiated ground motion can be deterministically modeled by substituting Equation 5 into Equations 7 and 8, for the *P*-wave and *S*-wave components respectively. Figure 8a shows an example of this, assuming random samples of isotropically distributed orientations, a log-raised cosine distribution for $(m)^{1/3}$ (similar to a truncated log-normal distribution) (Tsai et al., 2012), and uniformly distributed $\Delta t_k$. $N$ is chosen so that the largest size category has approximately 1,000 impacts. This number is expected to scale with the size of the fault zone, but each structure may also undergo multiple impacts, depending on how long slip continues for, and so $N$ also scales with total slip time (see Section 3.6).

Since the ground motions in Figure 8a are random, and it is unlikely that the force locations, orientations, amplitudes, and timings would ever be known deterministically in a realistic example, it is useful to characterize the ground motion contribution by its statistical features such as its spectrum, shown in Figure 8b. As described in Tsai and Hirth (2020), the spectrum is dominated by impacts of structures close to the 73rd percentile of the distribution, and the shape of the spectrum is well fit by the omega square model with high-frequency falloff rate $f^{-2}$. This behavior is expected since each of the force contributions from Equation 2 has a Brune-like omega square contribution (Tsai & Hirth, 2020). Moreover, the RMS ground motions in different directions are approximately equal, that is radiation is isotropic, as expected given the isotropic distribution of single forces. Note that while this model only includes a single corner, when superposed onto a frictional slip model appropriate at low frequencies, the spectrum may resemble a dual-corner model (Atkinson & Boore, 1995; Denolle & Shearer, 2016; Gusev, 2014; Ji & Archuleta, 2021) and low-frequency radiation is still expected to be the standard four-lobed double couple pattern expected of a shear source (Tsai & Hirth, 2020). Thus, we suggest that one may be able to distinguish between the models by observing whether this transition with increasing frequency from more four-lobed to more isotropic occurs as predicted by the impact model (even when scattering is minimal).

## 5. Conclusions

We have presented an analysis of how earthquake ground motions are produced when fault zone structure is complex, with a focus on specifically comparing the stochastic impact model of Tsai and Hirth (2020) with the single rough-fault frictional model of Dunham et al. (2011b), Shi and Day (2013) and Wollherr et al. (2018). The two models differ in many respects, ranging from their assumptions to various features of their ground motion predictions (see Table 1). Some of the most important differences that distinguish the impact model from the frictional model include: (a) a dependence on purely elastic physics whereas the frictional model depends not just on fault friction but also on off-fault viscoplastic parameters; (b) a requirement of a large number of fault-bounded blocks with a given statistical size and orientation distribution compared to the requirement of a single fault surface without sharp kinks in the frictional model; (c) predicted ground motions with a corner frequency that depends on fault-zone block ("particle") sizes in contrast to high-frequency radiation that depends on the off-fault viscosity in the frictional case; (d) predicted high-frequency radiation patterns that are isotropic for realistically complex fault zones compared to distinctly oriented radiation patterns for the frictional case; (e) predicted radiated energy with an $S/P$ ratio

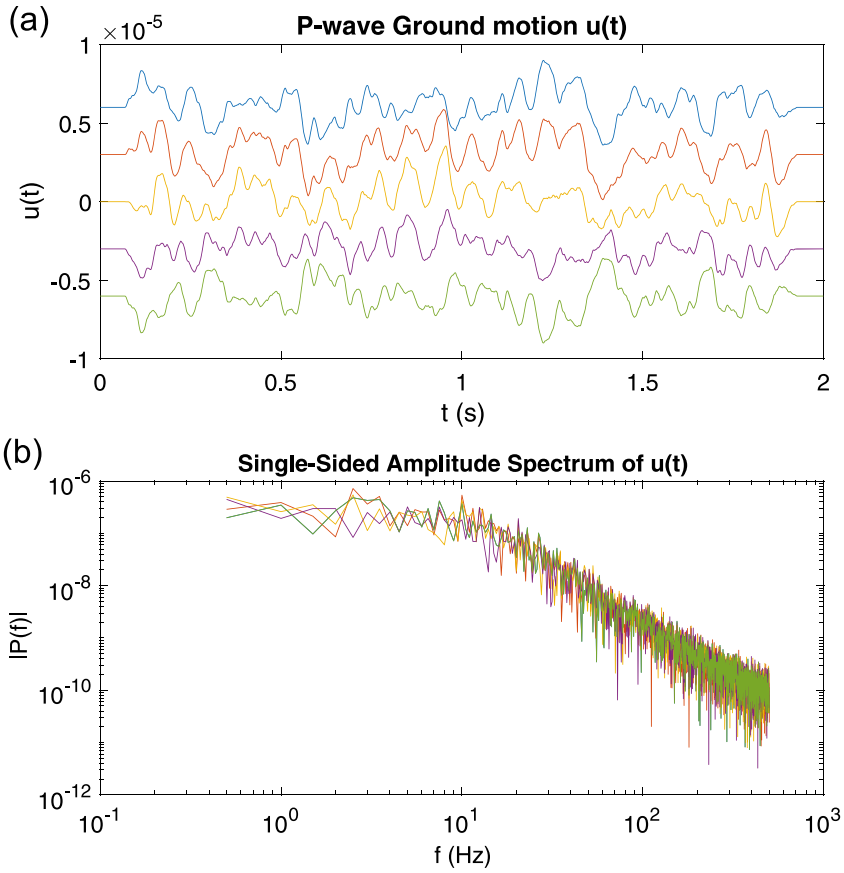


**Figure 8.** (a) Predicted *P* wave (radial) ground motions at 0°, 45°, 90°, 135°, and 180° relative to fault strike for one stochastic realization of the impact model. (b) Spectra for the 5 ground motions shown in (a).

of $(\alpha/\beta)^3$ instead of $(\alpha/\beta)^5$ (in the absence of scattering). Given the plausibility of both models and the many differences between them, it seems a worthwhile next step to consider whether the observational evidence supports, contradicts or otherwise distinguishes between the two models. Finally, while this study focuses on predicted ground motions for two end-member physical models, the physics of complex structural impacts may lead to different predicted earthquake rupture dynamics and energetics. It is beyond the scope of the present contribution to delve into these interesting implications, but we believe that examining such consequences would be a fruitful avenue for future work.

**Table 1**
*Summary of Key Model Differences*

| | Relevant regime | Cause of high-frequency radiation | Cause of additional[a] corner frequency, $f_c$ | High-frequency radiation pattern | Radiated energy |
|---|---|---|---|---|---|
| Elastic impact model | Large number of complex interacting faults | Near elastic collisions of fault structures | Timescale of structural impact, scales with structure size | Isotropic regardless of scattering | $\frac{E_S}{E_P} \sim \left(\frac{\alpha}{\beta}\right)^3$ |
| Rough fault frictional model | Small number of non-planar but smooth faults | Heterogeneous on-fault slip; off-fault viscoplastic deformation | Ratio of viscosity to elasticity; subfault size | Sum of double couples + CLVDs | $\frac{E_S}{E_P} \sim \left(\frac{\alpha}{\beta}\right)^5$ |

Abbreviations: $E_S$, *S*-wave energy; $E_P$, *P*-wave energy; CLVD, compensated linear vector dipole (Lay & Wallace, 1995).

[a]Corner frequencies described here are in addition to any corner frequencies that may exist due to earthquake rupture duration or rise time (e.g., on a planar fault).

## Data Availability Statement

No data were used in this article.

**Acknowledgments**
The authors thank the editor R. Abercrombie, associate editor Y. Huang, reviewer A. Elbanna and an anonymous reviewer for helpful suggestions. This work was supported by NSF EAR-1939227.

## References

Abercrombie, R. E. (2021). Resolution and uncertainties in estimates of earthquake stress drop and energy release. *Philosophical Transactions of the Royal Society A: Mathematical, Physical and Engineering Sciences*, *379*, 20200131. https://doi.org/10.1098/rsta.2020.0131

Aki, K. (1967). Scaling law of seismic spectrum. *Journal of Geophysical Research*, *72*, 1217–1231. https://doi.org/10.1029/jz072i004p01217

Allmann, B. P., & Shearer, P. M. (2009). Global variations of stress drop for moderate to large earthquakes. *Journal of Geophysical Research*, *114*, B01310. https://doi.org/10.1029/2008JB005821

Atkinson, G. M., & Boore, D. M. (1995). Ground motion relations for Eastern North America. *Bulletin of the Seismological Society of America*, *85*, 17–30.

Backus, G., & Mulcahy, M. (1976). Moment tensors and other phenomenological descriptions of seismic sources—I. Continuous displacements, *Geophysical Journal International*, *46*, 341–361. https://doi.org/10.1111/j.1365-246x.1976.tb04162.x

Bolton, D. C., Shreedharan, S., Riviere, J., & Marone, C. (2020). Acoustic energy release during the laboratory seismic cycle: Insights on laboratory earthquake precursors and prediction. *Journal of Geophysical Research*, *125*, e2019JB018975. https://doi.org/10.1029/2019jb018975

Bruhat, L., Klinger, Y., Vallage, A., & Dunham, E. M. (2020). Influence of fault roughness on surface displacement: From numerical simulations to coseismic slip distributions. *Geophysical Journal International*, *220*, 1857–1877. https://doi.org/10.1093/gji/ggz545

Brune, J. N. (1970). Tectonic stress and the spectra of seismic shear waves from earthquakes. *Journal of Geophysical Research*, *75*, 4997–5009. https://doi.org/10.1029/jb075i026p04997

Brune, J. N. (2001). Fault normal dynamic loading and unloading: An explanation for "non-gouge" rock powder and lack of fault-parallel shear bands along the San Andreas fault. In *AGU Fall Meeting Abstracts* S22B-0655. American Geophysical Union.

Campbell, C. S. (2003). A problem related to the stability of force chains. *Granular Matter*, *5*, 129–134. https://doi.org/10.1007/s10035-003-0138-6

Chester, F. M., & Chester, J. S. (1998). Ultracataclasite structure and friction processes of the Punchbowl fault, San Andreas system. California. *Tectonophys*, *295*, 199–221. https://doi.org/10.1016/s0040-1951(98)00121-8

Chester, F. M., & Chester, J. S. (2000). Stress and deformation along wavy frictional faults. *Journal of Geophysical Research*, *105*, 23421–23430. https://doi.org/10.1029/2000jb900241

Chester, F. M., Chester, J. S., Kirschner, D. L., Schulz, S. E., & Evans, J. P. (2004). Structure of large-displacement, strike-slip fault zones in the brittle continental crust. In G. D. Karner, B. Tyalor, N. W. Driscoll, & D. L. Kohlstedt (Eds.), *Rheology and deformation in the lithosphere at continental margins*. Columbia University Press.

Dahlen, F. A., & Tromp, J. (1998). *Theoretical global seismology*. Princeton University Press.

Daniels, K. E., & Hayman, N. W. (2008). Force chains in seismogenic faults visualized with photoelastic granular shear experiments. *Journal of Geophysical Research*, *113*, B11411. https://doi.org/10.1029/2008JB005781

Denolle, M. A., & Shearer, P. M. (2016). New perspectives on self-similarity for shallow thrust earthquakes. *Journal of Geophysical Research*, *121*, 6533–6565. https://doi.org/10.1002/2016jb013105

Dunham, E. M., Belanger, D., Cong, L., & Kozdon, J. E. (2011a). Earthquake ruptures with strongly rate-weakening friction and off-fault plasticity, part 1: Planar faults. *Bulletin of the Seismological Society of America*, *101*, 2296–2307. https://doi.org/10.1785/0120100075

Dunham, E. M., Belanger, D., Cong, L., & Kozdon, J. E. (2011b). Earthquake ruptures with strongly rate-weakening friction and off-fault plasticity, part 2: Nonplanar faults. *Bulletin of the Seismological Society of America*, *101*, 2308–2322. https://doi.org/10.1785/0120100076

Farin, M., Tsai, V. C., Lamb, M. P., & Allstadt, K. E. (2019). A physical model of the high-frequency seismic signal generated by debris flows. *Earth Surface Processes and Landforms*, *44*, 2529–2543. https://doi.org/10.1002/esp.4677

Faulkner, D. R., Lewis, A. C., & Rutter, E. H. (2003). On the internal structure and mechanics of large strike-slip fault zones: Field observations of the Carboneras fault in southeastern Spain. *Tectonophys*, *367*, 234–251. https://doi.org/10.1016/s0040-1951(03)00134-3

Frankel, A. (1991). High-frequency spectral falloff of earthquakes, fractal dimension of complex rupture, *b* value, and the scaling of strength on faults. *Journal of Geophysical Research*, *96*, 6291–6302. https://doi.org/10.1029/91jb00237

Graves, R., & Pitarka, A. (2016). Kinematic ground-motion simulations on rough faults including effects of 3D stochastic velocity perturbations. *Bulletin of the Seismological Society of America*, *106*, 2136–2153. https://doi.org/10.1785/0120160088

Gusev, A. A. (2014). Doubly stochastic earthquake source model: "Omega-square" spectrum and low high-frequency directivity revealed by numerical experiments. *Pure and Applied Geophysics*, *171*, 2581–2599. https://doi.org/10.1007/s00024-013-0764-9

Haskell, N. A. (1964). Total energy and energy spectral density of elastic wave radiation from propagating faults. *Bulletin of the Seismological Society of America*, *54*, 1811–1841. https://doi.org/10.1785/bssa05406a1811

Huang, Y., Ampuero, J.-P., & Helmberger, D. V. (2014). Earthquake ruptures modulated by waves in damaged fault zones. *Journal of Geophysical Research*, *119*, 3133–3154. https://doi.org/10.1002/2013jb010724

Huang, Y., Ampuero, J.-P., & Helmberger, D. V. (2016). The potential for supershear earthquakes in damaged fault zones—Theory and observations. *Earth and Planetary Science Letters*, *433*, 109–115. https://doi.org/10.1016/j.epsl.2015.10.046

Ji, C., & Archuleta, R. J. (2021). Two empirical double-corner-frequency source spectra and their physical implications. *Bulletin of the Seismological Society of America*, *111*, 737–761. https://doi.org/10.1785/0120200238

Kwiatek, G., & Ben-Zion, Y. (2013). Assessment of *P* and *S* wave energy radiated from very small shear-tensile seismic events in a deep South African mine. *Journal of Geophysical Research*, *118*, 3630–3641. https://doi.org/10.1002/jgrb.50274

Kwiatek, G., Goebel, T. H. W., & Dresen, G. (2014). Seismic moment tensor and *b* value variations over successive seismic cycles in laboratory stick-slip experiments. *Geophysical Research Letters*, *41*, 5838–5846. https://doi.org/10.1002/2014gl060159

Lay, T., & Wallace, T. C. (1995). *Modern global seismology*. Academic Press.

Lyakhovsky, V., & Ben-Zion, Y. (2020). Isotropic seismic radiation from rock damage and dilatancy. *Geophysical Journal International*, *222*, 449–460. https://doi.org/10.1093/gji/ggaa176

Ma, X., & Elbanna, A. (2019). Dynamic rupture propagation on fault planes with explicit representation of short branches. *Earth and Planetary Science Letters*, *523*, 115702. https://doi.org/10.1016/j.epsl.2019.07.005

Madariaga, R. (1976). Dynamics of an expanding circular fault. *Bulletin of the Seismological Society of America*, *66*, 639–666.

Mai, P. M., & Beroza, G. C. (2002). A spatial random field model to characterize complexity in earthquake slip. *Journal of Geophysical Research*, *107*, 2308. https://doi.org/10.1029/2001jb000588

McLaskey, G. C., & Glaser, S. D. (2011). Micromechanics of asperity rupture during laboratory stick slip experiments. *Geophysical Research Letters*, *38*, L12302. https://doi.org/10.1029/2011gl047507

Mitchell, T. M., Ben-Zion, Y., & Shimamoto, T. (2011). Pulverized fault rocks and damage asymmetry along the Arima-Takatsuki Tectonic Line, Japan. *Earth and Planetary Science Letters*, *308*, 284–297. https://doi.org/10.1016/j.epsl.2011.04.023

Ngo, D., Huang, Y., Rosakis, A., Griffith, W. A., & Pollard, D. (2012). Off-fault tensile cracks: A link between geological fault observations, lab experiments, and dynamic rupture models. *Journal of Geophysical Research*, *117*, B01307. https://doi.org/10.1029/2011JB008577

Nur, A. (2008). *Apocalypse: Earthquakes, archaeology, and the Wrath of God*. Princeton: Princeton University Press.

Okubo, K., Bhat, H. S., Rougier, E., Marty, S., Schubnel, A., Lei, Z., et al. (2019). Dynamics, radiation, and overall energy budget of earthquake rupture with coseismic off-fault damage. *Journal of Geophysical Research*, *124*, 11771–11801. https://doi.org/10.1029/2019jb017304

Ozawa, S., & Ando, R. (2021). Mainshock and aftershock sequence simulation in geometrically complex fault zones. *Journal of Geophysical Research*, *126*, e2020JB020865. https://doi.org/10.1029/2020jb020865

Reid, H. F. (1910). *The California earthquake of April 18, 1906. Report of the State Earthquake Investigation Commission, Volume II: The mechanics of the earthquake*. Washington DC: Carnegie Institution of Washington

Rempe, M., Mitchell, T., Renner, J., Nippress, S., Ben-Zion, Y., & Rockwell, T. (2013). Damage and seismic velocity structure of pulverized rocks near the San Andreas Fault. *Journal of Geophysical Research*, *118*, 2813–2831. https://doi.org/10.1002/jgrb.50184

Rice, J. R. (1983). Constitutive relations for fault slip and earthquake instabilities. *Pure and Applied Geophysics*, *121*, 443–475. https://doi.org/10.1007/bf02590151

Rice, J. R. (2006). Heating and weakening of faults during earthquake slip. *Journal of Geophysical Research*, *111*, B05311. https://doi.org/10.1029/2005jb004006

Rowe, C. D., & Griffith, W. A. (2015). Do faults preserve a record of seismic slip: A second opinion. *Journal of Structural Geology*, *78*, 1–26. https://doi.org/10.1016/j.jsg.2015.06.006

Rowe, C. D., Ross, C., Swanson, M. T., Pollock, S., Backeberg, N. R., Barshi, N. A., et al. (2018). Geometric complexity of earthquake rupture surfaces preserved in pseudotachylyte networks. *Journal of Geophysical Research*, *123*, 7998–8015. https://doi.org/10.1029/2018jb016192

SCEC (2014). *The turtle story, a native American account of earthquakes*. YouTube, Uploaded by SCEC. Retrieved from https://www.youtube.com/watch?v=8_83ppaxT74

Shi, Z., & Day, S. M. (2013). Rupture dynamics and ground motion from 3-D rough-fault simulations. *Journal of Geophysical Research*, *118*, 1122–1141. https://doi.org/10.1002/jgrb.50094

Sibson, R. H. (1986). Brecciation processes in fault zones: Inferences from earthquake rupturing. *Pure and Applied Geophysics*, *124*, 159–175. https://doi.org/10.1007/bf00875724

Swanson, M. T. (1988). Pseudotachylyte-bearing strike-slip duplex structures in the Fort Foster Brittle Zone, S. Maine. *Journal of Structural Geology*, *10*, 813–828. https://doi.org/10.1016/0191-8141(88)90097-1

Swanson, M. T. (2006). Pseudotachylyte-bearing strike-slip faults in mylonitic host rocks, Fort Foster brittle zone, Kittery, Maine. In: In R. Abercrombie, A. McGarr, G. Di Toro, & H. Kanamori (Eds.), *Earthquakes: Radiated energy and the physics of faulting, Geophysical Monograph Series* (Vol. 170). American Geophysical Union. https://doi.org/10.1029/170gm17

Takemura, S., Furumura, T., & Saito, T. (2009). Distortion of the apparent *S* wave radiation pattern in the high-frequency wavefield: Tottori-Ken Seibu, Japan, earthquake of 2000. *Geophysical Journal International*, *178*, 950–961. https://doi.org/10.1111/j.1365-246x.2009.04210.x

Templeton, E. L., & Rice, J. R. (2008). Off-fault plasticity and earthquake rupture dynamics. I: Dry materials or neglect of fluid pressure changes. *Journal of Geophysical Research*, *113*, B09306. https://doi.org/10.1029/2007jb005529

Tordesillas, A. (2007). Force chin buckling, unjamming transitions and shear banding in dense granular assemblies. *Philosophical Magazine*, *87*, 4987–5016. https://doi.org/10.1080/14786430701594848

Trugman, D. T., McBrearty, I. W., Bolton, D. C., Guyer, R. A., Marone, C., & Johnson, P. A. (2020). The spatiotemporal evolution of granular microslip precursors to laboratory earthquakes. *Geophysical Research Letters*, *47*, e2020GL088404. https://doi.org/10.1029/2020GL088404

Tsai, V. C., & Hirth, G. (2020). Elastic impact consequences for high-frequency earthquake ground motion. *Geophysical Research Letters*, *47*, e2019GL086302. https://doi.org/10.1029/2019GL086302

Tsai, V. C., Minchew, B., Lamb, M. P., & Ampuero, J.-P. (2012). A physical model for seismic noise generation from sediment transport in rivers. *Geophysical Research Letters*, *39*, L02404. https://doi.org/10.1029/2011GL050255

Tullis, T. E. (2015). Mechanisms for friction of rock at earthquake slip rates. In G. Schubert (Ed.), *Treatise on geophysics* (2nd ed., pp. 139–159). Elsevier. https://doi.org/10.1016/B978-0-444-53802-4.00073-7

Ulrich, T., Gabriel, A.-A., Ampuero, J.-P., & Xu, W. (2019). Dynamic viability of the 2016 Mw 7.8 Kaikoura earthquake cascade on weak crustal faults. *Nature Communications*, *10*, 1213. https://doi.org/10.1038/s41467-019-09125-w

Wollherr, S., Gabriel, A.-A., & Uphoff, C. (2018). Off-fault plasticity in three-dimensional dynamic rupture simulations using a modal Discontinuous Galerkin method on unstructured meshes: Implementation, verification and application. *Geophysical Journal International*, *214*, 1556–1584. https://doi.org/10.1093/gji/ggy213

Xu, S., Ben-Zion, Y., Ampuero, J.-P., & Lyakhovsky, V. (2015). Dynamic ruptures on a frictional interface with off-fault brittle damage: Feedback mechanisms and effects on slip and near-fault motion. *Pure and Applied Geophysics*, *172*, 1243–1267. https://doi.org/10.1007/s00024-014-0923-7